A&A 418, 347–356 (2004)
DOI: 10.1051/0004-6361:20040025

Astronomy & Astrophysics

65 Cybele in the thermal infrared: Multiple observations and thermophysical analysis⋆

T. G. Müller[1] and J. A. D. L. Blommaert[2]

[1] Max-Planck-Institut für extraterrestrische Physik, Giessenbachstraße, 85748 Garching, Germany
e-mail: tmueller@mpe.mpg.de
[2] Katholieke Universiteit Leuven, Instituut voor Sterrenkunde Celestijnenlaan 200B, 3001 Leuven, Belgium
e-mail: joris.blommaert@ster.kuleuven.ac.be

Received 19 May 2003 / Accepted 15 January 2004

Abstract. We investigated the physical and thermal properties of 65 Cybele, one of the largest main-belt asteroids. Based on published and recently obtained thermal infrared observations, including ISO measurements, we derived through thermophysical modelling (TPM) a size of 302 × 290 × 232 km (±4%) and an geometric visible albedo of 0.050 ± 0.005. Our model of a regolith covered surface with low thermal inertia and "default" roughness describes the wavelengths and phase angle dependent thermal effects very well. Before/after opposition effect and beaming behaviour can be explained in that way. We found a constant emissivity of 0.9 at wavelengths up to about 100 μm and lower values towards the submillimetre range, indicating a grain size distribution dominated by 200 μm particle sizes. The spectroscopic analysis revealed an emissivity increase between 8.0 and 9.5 μm. We compared this emissivity behaviour with the Christiansen features of carbonaceous chondrite meteorites, but a conclusive identification was not possible. A comparison between the Standard Thermal Model (STM) and the applied TPM clearly demonstrates the limitations and problems of the STM for the analysis of multi-epoch and -wavelengths observations. While the TPM produced a unique diameter/albedo solution, the calculated STM values varied by ±30% and showed clear trends with wavelength and phase angle. 65 Cybele can be considered as a nice textbook case for the thermophysical analysis of combined optical and thermal infrared observations.

Key words. minor planets, asteroids – radiation mechanisms: thermal – infrared: solar system

1. Introduction

The asteroid 65 Cybele is a main-belt asteroid and the main representative of a group of asteroids with semi-major axis in the range $3.27 < a < 3.70$ AU, eccentricities $e \leq 0.30$ and inclinations of $i \leq 25°$ (Gradie et al. 1989). 65 Cybele is generally considered as one of the 10 largest asteroids, with a published diameter between 230 (Dobrovol'skij 1980; Taylor 1981) and about 330 km (Green et al. 1985). Although discovered in 1863, it took until 1980 before its rotational properties were determined as one of the last remaining large minor planets (Schober et al. 1980). Recent analysis of many lightcurve observations lead to a rotation period of about 6 h, a unique spin vector solution pair with a retrograde sense of rotation and an elongated body shape (Erikson 2000).

Based on its low albedo and the flat to slightly reddish spectrum in the 0.3 to 1.1 μm range, it was classified as P-type object (Tholen 1989) and due to a weak ultraviolet absorption feature short ward of 0.4 μm as C0-type (Barucci et al. 1987). Recently Bus (1999) classified 65 Cybele as Xc type, based on reflectance spectra covering the wavelength interval from 0.44 to 0.92 μm. These taxonomic types indicate hydrated silicates, carbon and organics on the asteroids surface (Gaffey et al. 1989).

Another interesting aspect comes from the occultation measurement: Dobrovol'skij (1980) reported a second event during the occultation of AGK3 +19 599 which was attributed to a satellite of 11 km diameter, located 917 km from the center of 65 Cybele (in the case of a central occultation). So far, no confirmation of the satellite through other techniques was published. It was one of the targets in the HST search for binaries "Imaging Snapshots of Asteroids" Storrs et al. (1999) and Storrs (priv. comm.), but with unknown outcome so far. No radar measurements are available yet.

Tedesco & Veeder (1992) and Tedesco et al. (2002) derived from IRAS observations diameter and albedo values of 237.26 ± 4.2 km and 0.0706 ± 0.003, respectively. The only direct size information from the occultation event in 1979 resulted in a diameter of 230 ± 16 km, with a largest measured chord of 245 km (Dobrovol'skij 1980; Taylor 1981; Xiu-Yi 1979). Both values, the radiometric and the occultation diameter, agree nicely. But ground-based N-band observations (Morrison & Chapman 1976; Morrison 1977; Bowell et al. 1979; Green et al. 1985) lead to diameters larger than 300 km. The published radiometric diameters and albedos were all based on the concept of the Standard Thermal Model (STM;

Send offprint requests to: T. G. Müller,
e-mail: tmueller@mpe.mpg.de

⋆ Partly based on observations with ISO, an ESA project with instruments funded by ESA Member States (especially the PI countries: France, Germany, The Netherlands and the UK) and with the participation of ISAS and NASA.

Lebofsky et al. 1986; Lebofsky & Spencer 1989), but using different values for the infrared beaming parameter η, the phase angle correction and the emissivity. Using for example the STM η-value of 0.756 (Lebofsky et al. 1986) would lower some of the earlier 300 km diameter values to about 250 km, but the Green et al. (1985) values would still be close to 300 km. The higher phase angle correction of Bowell et al. (1979) would again increase the diamter of all measurements taken at large phase angles.

The diameter is the most fundamental parameter, but in case of 65 Cybele it has very large uncertainties, much larger than for other asteroids of comparable size. Where is this uncertainty coming from? Are the data sets too different or some of them unreliable? What role play the STM concept, the simplification in the shape, the missing thermal and rotation effects or the various other model input parameters?

The first thermal spectrum of 65 Cybele was published by Green et al. (1985). They did not see any pronounced emission features in the 8 to 13 μm wavelength range. In the years 1996–1998 65 Cybele was extensively observed by ISO with the scientific goal of providing new insights into the chemical composition and the mineralogy for a sample of main-belt asteroids. Are there any spectral features visible? If yes, what are the meteoritic and mineralogic counterparts?

With the availability of a recently established thermophysical model (TPM) by Lagerros (1996, 1997, 1998) we are now in a position to combine the information on the asteroid, its rotational behaviour, different observing and illumination geometries with the thermal measurements taken at different wavelengths and different times.

In the following, we show the results of the re-analysis and re-calibration of the existing thermal observations from ground- and satellite-based instruments, including photometric and spectroscopic measurements (Sect. 2). In Sect. 3 we present the basic parameters of our TPM analysis and derive radiometric diameters and albedos for all photometrically reliable data sets (Sect. 3.2). In the spectroscopic analysis (Sect. 3.3) we focused on the modelling of the shape of the thermal continuum emission which is strongly connected to thermal effects on a regolith covered surface. The TPM analysis section is followed by extensive discussions of radiometric and spectroscopic results (Sect. 4). We used a large sample of infrared observations, spanning a wide range of phase angles and wavelengths, to demonstrate the possibilities and limitations of the thermophysical modelling of asteroids (Sect. 5).

2. Observations in the Thermal Infrared

2.1. Re-analysis of previous measurements

TRIAD observations

The original TRIAD[1] fluxes were based on three 65 Cybele observations from March 18, 1975, 08:24 UT, with an average N-band magnitude of +0.85 ± 0.05 mag (Morrison & Chapman 1976). We used the Rieke et al. (1985) absolute photometric system for the standard stars to re-calibrate this flux. This led to a new N-band value of +0.92 mag, corresponding to a colour corrected flux at 10.6 μm of 14.55 ± 0.87 Jy (measurement and calibration errors have been added quadratically).

IR spectroscopy from UCL

Green et al. (1985) presented the first 8- to 13 μm spectrum of 65 Cybele. It was taken on April 18, 1982 and calibrated against α Boo. We re-calibrated the 10.0 μm flux value to 25.5 ± 2.9 Jy with the Cohen et al. (1995) model for α Boo (the Green et al. value for α Boo is 15.0% higher than the Cohen et al. value at 10.0 μm). The re-calibration resulted in flux values of 14.4 ± 2.0 Jy at 8.5 μm, 25.5 ± 2.9 Jy at 10.0 μm and 50.9 ± 4.4 Jy at 12.0 μm for the given epoch.

IRAS observations

IRAS (Beichman et al. 1988) scanned 6 times over 65 Cybele, each time with all 4 wavelength bands. The latest flux values and the corresponding analysis were presented by Tedesco et al. (2002). We used the colour corrected monochromatic IRAS fluxes (without applying the STM-related band-to-band corrections) for our reanalysis (see also Müller & Lagerros 1998).

IRTF observations

We included in our analysis 3 IRTF measurements (D. Osip, priv. communications, see Table 1).

No observational or calibration errors were given, but the data were considered as a high accuracy dataset (Osip, priv. comm.). We assumed a 10% flux uncertainty for the N-band and 15% for the Q-band photometry.

Table 1. IRTF observations of 65 Cybele from Dec. 19, 1996.

Julian date	λ_c [μm]	Flux [Jy]
2 450 436.71813	10.5	7.0
2 450 436.72042	10.5	6.7
2 450 436.72350	18.0	17.8

UKIRT observations

The UKIRT mid-IR N- and Q-band data of 65 Cybele have been obtained in August 1996 with the MPIA 5–25 μm camera MAX (Robberto & Herbst 1998). Observations, data reduction and calibration are described in Müller & Lagerros (1998).

ISOPHOT photometric data

65 Cybele was measured at wavelengths between 65 and 200 μm with ISOPHOT (Lemke et al. 1996) at 3 different observing epochs. Observations, data reduction and calibration are discussed in Müller & Lagerros (1998, 2002).

2.2. ISOPHT PHT-S measurement

The observational details of the PHT-S measurements are given in Table 2. The PHT-S short wavelength part (2.47–4.87 μm) covers the transition between reflected light and thermal

[1] Tucson revised Index of Asteroid Data.

Table 2. PHT-S, CAM CVF and CAM filter observations of 65 Cybele. OTT is the On Target Time.

Instrument	TDT	Start observation	λ-range [μm]	OTT [s]	Field of view
PHT-S	37 300 324	23-Nov.-96 12:40:26	5.84–11.62	364	$24'' \times 24''$
CAM-CVF forward (down)	77 002 401	25-Dec.-97 02:08:41	17.00–4.96	2996	$96'' \times 96''$
CAM-Filter	77 002 402	25-Dec.-97 02:59:19	6.0–14.9	3118	$48'' \times 48''$
CAM-CVF backward (up)	77 002 403	25-Dec.-97 03:52:01	5.02–17.00	2970	$96'' \times 96''$

emission. It has been excluded in our thermophysical analysis. The data reduction of the 5.84–11.62 μm part was done in a standard way, using PIA[2] (for details of the PHT-S data reduction steps see Dotto et al. 2002). There was no dedicated background measurement, we therefore used COBE-DIRBE measurement results (Hauser et al. 1998) as replacement. The color corrected, weekly maps from the COBE-DIRBE data sets were adjusted for the PHT-S beam size. The two DIRBE values at 4.9 and 12 μm were then connected using a 266 K blackbody (Ábrahám et al. 1999) and subtracted from the measured spectrum of 65 Cybele. The background contribution was between 4 and 10% in the PHT-S wavelength range.

Figure 1 shows the reduced and background subtracted result of the PHT-S observation together with the corresponding TPM prediction. Typical signal processing uncertainties were between 2 and 6%. The absolute calibration error for bright point-like sources in staring mode is less than 10% (Laureijs et al. 2002). For our analysis we added quadratically the individual signal processing errors and an absolute calibration error of 5%. The lower part of Fig. 1 shows the ratio between the observed spectrum and the TPM prediction (see Sect. 3).

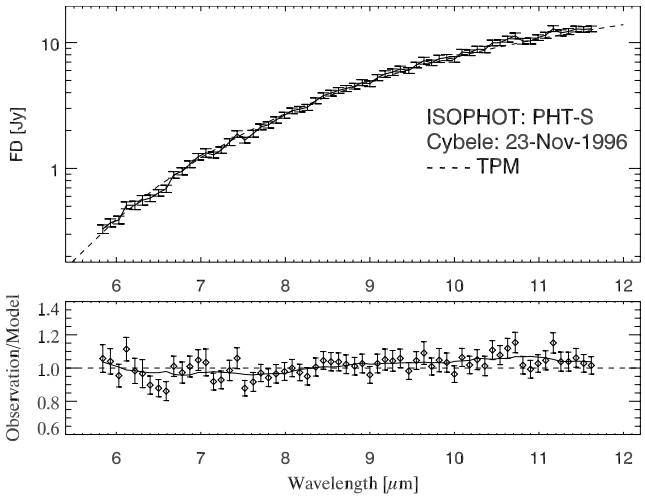

Fig. 1. PHT-S spectrum of 65 Cybele. The TPM prediction is plotted as dashed line (with $D_{\rm eff}$ = 296.5 km, p_V = 0.043 and default thermal parameters as described in Sect. 3.1). The error bars are the signal processing errors (between 2 and 6%) added quadratically to the assumed calibration error of 5% per pixel. The solid line in the lower part was produced through a 10 element smoothing of the PHT-S to TPM ratio (see Sect. 3).

[2] ISOPHOT Interactive Analysis.

2.3. ISOCAM CVF and filter observations

On Christmas day 1997, a for- and backward scan was performed in the 5 to 17 μm wavelength range with the ISOCAM Circular Variable Filter (CVF) (Cesarsky et al. 1996). The scan was performed skipping one CVF position per CVF step, corresponding to steps of approximately 0.2 μm for the 9−17 μm and 0.1 μm for the shorter wavelength range. The pixel field of view was 3″ leading to a total field of view of 96″. The data reduction was done within the CAM Interactive Analysis package (Ott et al. 1997) and followed the same strategy as was done for the standard stars observations, used for the calibration of the Spectral Response Function (Blommaert et al. 2001). The flux calibration was done using the OLP v10 SRF[3]. Aperture photometry was applied avoiding the contribution from reflected light on the detector (Blommaert et al. 2001). The strategy of combining a for- and backward scan allows to check observed spectral features and also allows to a certain extent the correction of the ISOCAM transient response. We applied the Fouks-Schubert method (Coulais & Abergel 1996) to correct the transient of the signal. The CVF scan starting at 5 μm after the fixed filter measurements suffers strongly from a remnant which is not corrected for by the transient correction method. For this reason we judge the data for 5−7 μm in the up-scan as less reliable.

In the time between the two CVF scans nine fixed filter measurements were performed in the 6–15 μm wavelength range. The zodiacal background becomes important at wavelengths longer than 9 μm. Therefore, dedicated background measurements were done in the long-wavelength filters. They were performed before 65 Cybele itself was observed to avoid remnants of the 65 Cybele measurement because of the transients. The on-source measurements were long enough to allow stabilisation of the signal so that no correction had to be applied (Blommaert et al. 2000). The obtained flux densities have been colour corrected using the average CVF as input spectrum.

The resulting monochromatic flux densities are listed in Table 3. These values are also plotted together with error bars in Fig. 2. The lower part of the figure shows the ratio between the observed CAM filter values and the corresponding TPM prediction (see Sect. 3).

2.4. ESO-TIMMI2 N- and Q-band observations

We obtained additional N- and Q-band observations of 65 Cybele using the TIMMI2 camera (Reimann et al. 2000),

[3] Off Line Processing version 10, Spectral Response Function.

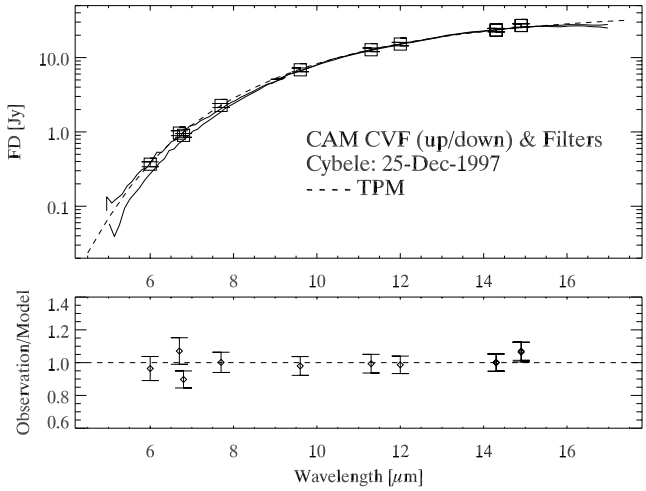

Fig. 2. CAM-CVF and CAM filter observations of 65 Cybele. The TPM prediction is plotted as dashed line (with $D_{\rm eff}$ = 278.8 km, p_V = 0.049 and default thermal parameters as described in Sect. 3.1). The lower part shows the resulting CAM filter flux densities divided by the corresponding TPM prediction (see Sect. 3).

Table 3. ISOCAM filter measurements. The monochromatic flux values are background subtracted and colour corrected. The 1-σ errors of the photometry are between 1 and 4%. The colour correction terms (Col. CC) have been determined from the averaged CVF-spectrum. CVF uncertainties produce errors in the colour correction values of about 5% in the *LW*4 and *LW*2 filters and about 1% for the others. The uncertainty in flux conversion is approximately 5%. All errors have been added quadratically (Col. "Error"). The measurements were taken on 25 December 1997 between 3:00 and 3:50 UT.

Filter	$\lambda_{\rm ref}$ [μm]	CC	Flux [Jy]	Error [Jy]
*LW*4	6.0	1.08	0.368	0.028
*LW*2	6.7	1.32	0.964	0.073
*LW*5	6.8	1.00	0.899	0.052
*LW*6	7.7	1.06	2.27	0.14
*LW*7	9.6	1.03	6.85	0.40
*LW*8	11.3	1.01	12.74	0.73
*LW*10	12.0	0.91	15.20	0.82
*LW*3	14.3	0.99	23.49	1.25
	14.3	0.99	23.39	1.22
*LW*9	14.9	1.00	27.09	1.42
	14.9	1.00	26.92	1.50

mounted on the ESO-La Silla 3.6 m telescope. Table 4 summarises the observational results[4].

We did a standard data reduction for the chopping-nodding imaging mode. Asteroid and calibration star measurements have been taken within 30 min, all *N*1 integration time were 144 s, the *Q*1 integration times were 108 s. The relatively large uncertainties in Table 4 are due to the variable atmospheric conditions. The flux errors are estimates based on the monitoring of the reference stars. No colour or airmass correction was performed, both effects are only on a 1−2% level and much smaller than the photometric errors.

[4] Based on observations collected at the European Southern Observatory, Chile; ESO, No. 69.C-0090.

Table 4. Summary of the ESO-TIMMI2 *N*- and *Q*-band observations. All measurements were taken between airmass 1.02 and 1.24. The calibration stars were HD 178345 and HD 169916, with model spectra from Cohen et al. (1999).

Date (UT)	Time	Filter	$\lambda_{\rm ref}$ [μm]	Flux [Jy]	Error [Jy]
10-Jun.-02	07:42	*Q*1	17.75	74.9	$\pm^{3}_{15}$
11-Jun.-02	08:47	*Q*1	17.75	57.4	5.0
	08:51	*Q*1	17.75	57.7	5.0
	10:02	*N*1	8.60	8.8	0.5

3. Thermophysical model analysis

We applied the thermophysical model (TPM) developed by Lagerros (1996, 1997, 1998) and extensively used and refined by Müller & Lagerros (1998, 2002). The TPM includes shape, rotational behaviour and thermal behaviour of a given asteroid at the specific observing and illumination geometry. It allows to derive radiometric sizes and albedos from thermal infrared observations, taking shape information, geometry and thermal aspects into account.

3.1. Model input values

The H[5] and G[6] values are taken from Lagerkvist & Magnusson (1990), with $H = 6.70 \pm 0.15$ as the weighted mean value of four apparitions and $G = 0.09 \pm 0.05$. Erikson (2000) presented a good quality solution pair for the spin vector based on a retrograde sense of rotation and a synodic rotation period of 6.1 h (see Table 5). However, due to noisy and under-sampled input data, the spin vector pair is still considered only as class II, indicating that higher quality data might improve the situation.

The sense of rotation can in principle be determined from the anlysis of thermal observations before and after opposition (e.g. Müller 2002). In cases where two spin vector solutions with different senses of rotation are given, the thermophysical analysis allows to determine the correct one. But to distinguish between two spin vector solutions with the same sense of rotation is very difficult on basis of infrared data. The before-/after opposition effect is then not very pronounced. Our TPM analysis for 65 Cybele gave almost identical diameter and albedo values for both spin vector solutions. For the first solution (first line in Table 5) we obtained a slightly smaller standard deviation around the mean diameter and albedo values. Therefore we accepted solution 1 for all following calculations. The corresponding ellipsoidal shape model solution is closely connected to this spin vector solution.

The determination of thermophysical quantities such as thermal inertia, beaming parameters or emissivity require large samples of infrared measurements (Müller & Lagerros 1998), but for regolith covered, large main-belt asteroids, default thermal values seem to work fine (Müller et al. 1999). They found a thermal inertia value of $\Gamma = 15$ J m^{-2} s$^{-0.5}$ K^{-1} for 1 Ceres which they also used successfully for other main-belt asteroids

[5] Absolute magnitude in the $H - G$ magnitude system.

[6] V-band slope parameter in the $H - G$ magnitude system.

Table 5. Spin vector parameters of 65 Cybele (Erikson 2000).

Asteroid	Spin vector		Sidereal period	Absolute rotational phase	Ellipsoidal model	
	λ_0	β_0	$P_{\rm sid}$	γ_0	a/b	b/c
65 Cybele	56 ± 15	−25 ± 15	0.2572901 ± 0.0000004	−38° at T_0 = 2 446 420.5	1.04 ± 0.05	1.25 ± 0.10
	237 ± 15	−16 ± 15	0.2572901 ± 0.0000004	−36° at T_0 = 2 446 420.5	1.04 ± 0.05	1.24 ± 0.10

(Müller & Lagerros 2002). We adopted this Γ-value, as well as the derived beaming model parameters $f = 0.6$ (fraction of surface covered by craters) and $\rho = 0.7$ (rms of the surface slopes). These beaming values correspond roughly to the "default" STM beaming parameter (Lebofsky et al. 1986) if the heat conduction is neglected (Lagerros 1998). For the emissivity we used a constant value of $\epsilon = 0.9$ at all wavelengths between the near-IR and 100 μm. At longer wavelengths we used a wavelength dependent emissivity with decreasing values from 0.9 at 100 μm to 0.8 at 400 μm.

3.2. Radiometric analysis

Based on TPM parameters from Sect. 3.1, we derived radiometric effective diameter and albedo values from all photometric and spectroscopic measurements in Sect. 2. The results are given in Table 6.

The typical observational and calibrational errors of individual measurements are between 5 and about 20% in flux density. The translation into diameter leads to 3 to 10% uncertainties for individual radiometric diameters. A 10% change in radiometric diameter for 65 Cybele requires an albedo modification of 0.010 (a larger diameter requires a lower albedo and vice versa). The $D_{\rm eff}$ values per instrument are within ±8% of the weighted mean, only the UKIRT value is significantly off for unknown reasons. The ISOPHOT data were taken under the same aspect angles as the UKIRT data, but do not show such high $D_{\rm eff}$ values. The highest quality photometric data are the CAM filter measurements. The derived diameter and albedo values are very close to the weighted mean values of all 10 sets of independent observations.

The effective diameters are connected to the shape model via the equal volume sphere formula $D_{\rm eff} = 2(abc)^{1/3}$ (see also Müller & Lagerros 1998). Shape, object orientation (represented by spin vector and aspect angle[7]), illumination, rotation and thermal effects are taken into account in the calculation of $D_{\rm eff}$ and p_V. The calculated weighted mean effective diameter of 273.0 km corresponds to an absolute ellipsoidal size of $2a \times 2b \times 2c = 301.9 \times 290.3 \times 232.2$ km for the given spin vector solution (first line in Table 5).

3.3. Spectroscopic analysis

The original idea of the spectroscopic observations was to get new insides into the chemical composition and mineralogy of this main-belt asteroid. Mainly the nature of silicate features can be studied in the wavelength range between 8 and 12 μm (Dotto et al. 2000). Green et al. (1985) found no prominent emission features in the N-band spectrum of 65 Cybele.

Dotto et al. (2002) and Barucci et al. (2002) analysed the spectroscopic features by dividing the observed spectrum by the corresponding TPM prediction under the assumption of a perfect emissivity at all wavelength ($\epsilon = 1.0$). Here, we follow this procedure. Figure 3 shows the PHT-S and the CAM-CVF measured spectrum divided by the corresponding TPM with $\epsilon = 1.0$. Both spectra agree in spectral shape within the given observational and instrumental uncertainties.

The PHT-S spectrum (Fig. 1) was derived from 64 individual pixels which have a completely independent calibration for each pixel. The PHT-S data are therefore not ideal for an analysis of very low level spectroscopic features. The CAM-CVF scans are much better suited for such an analysis. The source is always seen by the same pixels and with the variable filters the source spectrum is scanned. Despite the disadvantages of the PHT-S spectrum for the analysis of shallow features, a 10 element smoothed PHT-S spectrum resembles the CVF spectrum very well.

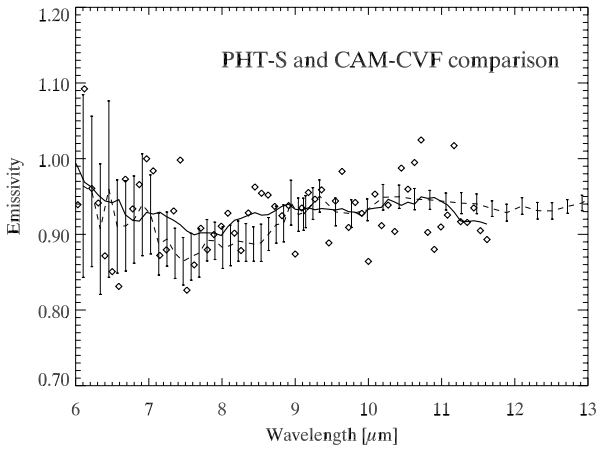

Fig. 3. Comparison between PHT-S (diamonds) and CAM-CVF (dashed line with error bars) spectra divided by the corresponding TPM predictions with $\epsilon = 1.0$. The solid line was produced by a 10-element smoothing of the PHT-S emissivity values. The CAM-CVF is the average of the up and down scans divided by the model prediction.

4. Discussion

4.1. Physical parameters

Our reanalysis of 10 independent data sets (see Sect. 2) give now very consistent radiometric result through the TPM. We determined the effective diameter to $D_{\rm eff} = 273.0 \pm 12.0$ and

[7] Angle between the rotation axis of 65 Cybele and the radius vector to Earth.

Table 6. $D_{\rm eff}$ and p_V values, together with the standard deviation of all calculated values per instrument (for TRIAD only the flux uncertainty has been taken into account). The values have been derived through the TPM with default input parameters for shape and thermal behaviour (see Sect. 3.1).

Instr. (# of Obs)	λ [μm]	Asp. [°]	$D_{\rm eff}$ [km]	p_V
Photometry				
TRIAD (1)	N-band	70	256.4 ± 7.5	0.058 ± 0.003
IRAS (24)	12, 25, 60, 100	68–71	262.4 ± 14.0	0.056 ± 0.006
UKIRT (4)	N- and Q-band	87	(329.1 ± 19.9)	(0.035 ± 0.004)
IRTF (3)	N- and Q-band	94	281.5 ± 15.7	0.048 ± 0.006
PHT-P/C (13)	60...200	85–94	269.2 ± 10.0	0.053 ± 0.004
CAM Fil (11)	6.0...14.9	144	278.8 ± 7.0	0.049 ± 0.003
TIMMI2 (4)	8.6, 17.75	66	260.5 ± 19.2	0.057 ± 0.008
Spectroscopy				
IRSPEC (3)	8.5, 10.0, 12.0	26	264.8 ± 9.6	0.054 ± 0.004
PHT-S (12)	6.0...11.5 (0.5 μm steps)	89	296.5 ± 8.3	0.043 ± 0.002
CAM-CVF (15)	7.5...14.5 (0.5 μm steps)	144	273.8 ± 7.5	0.051 ± 0.003
Weighted Mean values:			273.0 ± 11.9	0.050 ± 0.005

the albedo to $p_V = 0.050 \pm 0.005$. The discrepancy to the Tedesco et al. (2002) results is mainly related to the spherical shape simplification of the STM. Thermal effects, the beaming model, phase angle corrections and band-to-band corrections also contribute to the deviations. The occultation diameter was derived from a circle fitted to 3 measured chords. The uncertainties of the measurements and the limited information from a 3-chord occultation event also allow for a fit with a larger slightly elongated ellipse, corresponding to the projected cross section of our derived radiometric size values. The fact that different data sets, taken at different wavelengths, different observing and illumination geometries give now one consistent solution is certainly in favor of our larger diameter. And, all IRAS observations fit nicely into that picture, including the 100 μm data which were not used for the Tedesco et al. (2002) calculations. Here, we would like to emphasize that we did not apply any band-to-band corrections or any other wavelengths-, phase angle or beaming corrections, like it was done for the STM IRAS applications.

Despite the usage of best available ellipsoidal shape model and the nice agreement on average between the TPM and the observations, we believe that the unknowns of the true shape limit the accuracy of TPM predictions for individual epochs. Deviations between the true object cross section and the projected model cross section are easily possible, but so far no improved shape model (e.g. from radar or direct imaging methods) is available.

The shape model is only useful together with the spin vector solution. Erikson (2000) gives 2 solutions as result of lightcurve inversion methods (see Table 5), but both solutions have the same sense of rotation. The determination of the correct solution on basis of radiometric analysis is therefore very difficult (see Sect. 3.1 for details). Here, we accepted solution 1 for all calculations.

4.2. Thermal parameters

We used a flat emissivity model with $\epsilon = 0.9$ over all wavelengths out to 100 μm, at longer wavelengths the model emissivity is slowly decreasing towards values of 0.8 at sub-mm wavelength. Previously published emissivity values of 1.0 at around 20 μm were based on ground-based Q-band observations and IRAS 25 μm fluxes together with very uncertain beaming values (Müller & Lagerros 1998). With our modification of taking a constant 0.9 value at mid-IR wavelengths we investigate the emissivity behaviour in this critical region where beaming effects play an important role (Dotto et al. 2000). In Fig. 4 there is no trend with wavelength visible out to about 150 μm. The constant "observation over TPM" ratios in Figs. 1 and 2 confirm our assumption of a constant $\epsilon = 0.9$ at mid-IR wavelengths. The 5 ISOPHOT measurements at wavelength beyond 150 μm (calibrated against a few stars and the planets Uranus and Neptune) show fluxes which are about 10% lower than the TPM predictions (Fig. 4). Müller & Lagerros (2002) see nice agreement with this current emissivity model for 1 Ceres, 2 Pallas, 4 Vesta and 10 Hygiea out to 200 μm, although for 2 Pallas and 4 Vesta there were indications for a similar trend at the very longest wavelengths. The observed far-IR fluxes are to a good approximation directly proportional to the hemispherical model emissivity (Müller & Lagerros 1998). Instead of a slow decrease from 0.9 at 100 μm to 0.8 at 400 μm, the 65 Cybele observations now indicate a more abrupt decrease in emissivity to values around 0.7−0.8 in the wavelength range 150 to 200 μm.

Redman et al. (1992, 1998) found effective emissivities between 0.5 and 0.9 in the sub-mm range for 7 large asteroids. They attribute differences in the emissivity behaviour to different optical depth of the warm surface material and its density. Scattering processes by grains within the regolith reduce the emissivity in a wavelength dependent fashion. For the Moon the far-IR emission is also suppressed by scattering processes

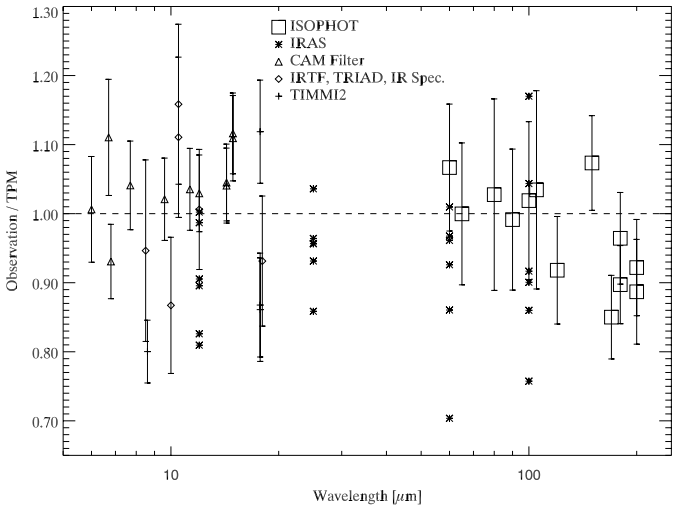

Fig. 4. The observation over TPM ratios for the photometric measurements plotted against the corresponding wavelengths (see Fig. 7 for STM ratios). The IRAS values are given without error bars for clarity. All TPM calculations were done with the resulting weighted mean values from Table 6.

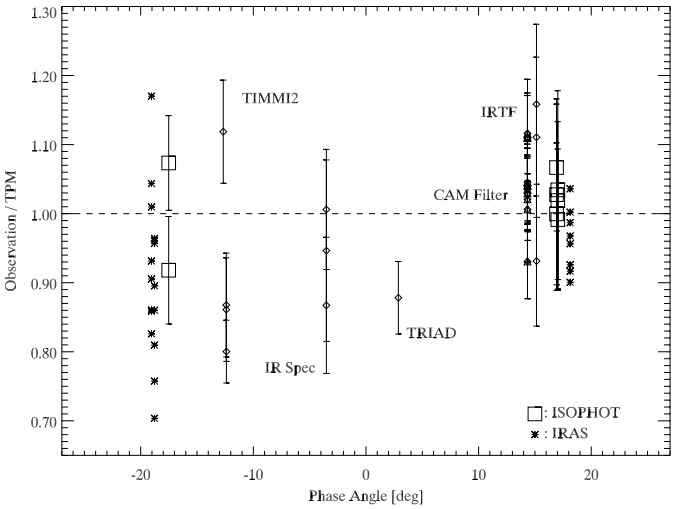

Fig. 5. The observation over TPM ratios for the photometric measurements plotted against the corresponding phase angles. All TPM calculations were done with the resulting weighted mean values from Table 6.

(Simpson et al. 1981). Scattering processes are most effective if wavelength and grain sizes have similar dimensions. Following this interpretation, our far-IR low emissivities indicate that the dominant particle size in the 65 Cybele's regolith (and maybe also for 2 Pallas and 4 Vesta) would be around 200 μm. More observations are needed to identify the precise emissivity behaviour. Well-calibrated spectroscopic observations in the far-IR and sub-millimetre (e.g. with HERSCHEL) will then allow a detailed description of particle size distributions within the regolith.

The measurements before and after opposition come from different instruments and are too inhomogeneous to identify clear trends with phase angle, especially as the measurements before opposition (negative phase angle) have too large error bars. We varied the thermal inertia between 0 and 50 J m^{-2} s$^{-0.5}$ K^{-1} to study the systematic changes in the data representation of Fig. 5. The zero thermal inertia produces a significantly larger scatter in the observation-to-model ratios. The $\Gamma = 50$ calculations showed a very pronounced asymmetry between before and after opposition ratios. Our default value of 15 J m^{-2} s$^{-0.5}$ K^{-1} seems to work fine, but somewhat smaller or larger values cannot be excluded. The much larger scatter in the before opposition ratios is pure coincidence. E.g. the before opposition IRAS data cover a much larger range in flux and the most deviating IRAS ratios on the left side of Fig. 5 belong to the lowest measured fluxes.

The beaming model with $\rho = 0.7$ and $f = 0.6$ influences strongly the slope of the observation to model ratios in the mid-IR (Dotto et al. 2000). The flat curves in Figs. 1 and 2 confirm our "default beaming model". About 10–20% modifications of the rms slope value (ρ) and the fraction of surface covered by craters (f) would still be in agreement with the PHT-S and the CAM filter measurements. Müller (2002) demonstrated in different model simulations the influences of the thermal parameters with wavelength and phase angles. But thermal inertia, beaming effects and the low level mineralogic emission features play together and influence the slope of the thermal emission in a complicated way and the different contributions are not easy to disentangle.

4.3. Emissivity analysis

Barucci et al. (1987) classified 65 Cybele as C0-type asteroid on basis of visual multi-color and IRAS data. They associated this taxonomic type with carbonaceous chondrites. The asteroids 10 Hygiea and 511 Davida, also C0-types, were found to show similarities in near-IR and 3 μm spectroscopy with carbonaceous chondrite meteorites of CI/CM subclass (Hiroi et al. 1996). Therefore, we concentrated our search for meteoritic analogues to carbonaceous chondrites, which represent, chemically and mineralogically, the most primitive material in the solar system.

In Fig. 6 we show the average CVF scan (divided by a TPM prediction with $\epsilon = 1.0$) with the error bars derived from the two CVF scans ($\sigma_{\rm mean}/\sqrt{2}$). For comparison, we plotted the emissivity of different powdered stony meteorite samples, representing 17 carbonaceous chondrite meteorites at small particle sizes of 0–75 μm (Salibury et al. 1991a,b; ASTER spectral library[8]). This library contains 60 meteorite samples all at grain sizes of 0–75 μm. The sample includes five meteorites of subclass CI, five of subclass CM, five of subclass CO and two of subclass CO3. The emissivity spectra (1 – measured reflectivity) are offset for clarity.

The 65 Cybele emissivity shows no prominent features, but an increase in emissivity between 8.0 and 9.5 μm is seen in both down and upward CVF scans and is thus a reliable feature, contrary to the part below 7.0 μm where the source becomes weak and transient problems hamper the measurement (see Sect. 2.3). Between 12.5 and 14 μm we recognise a very shallow feature which is also present in both scans.

[8] http://speclib.jpl.nasa.gov

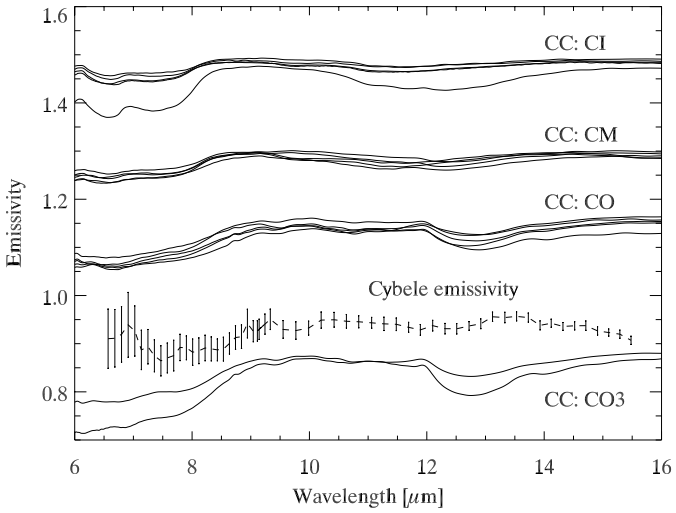

Fig. 6. The average CAM-CVF scan was divided by a TPM prediction with model emissivity set to 1.0 at all wavelengths. The average CVF/TPM ratio is plotted as dashed line. The 65 Cybele emissivity curve shows no prominent features in the 7 to 15 μm range. Different carbonaceous chondrites are shown for comparison and vertically shifted for clarity.

Salibury et al. (1991a) noted that a rather steep increase in emittance, the so-called Christiansen feature (CF), occurs between the wavelength region dominated by volume scattering (roughly below 7.5 μm) and the wavelength region dominated by surface scattering and reststrahlen bands (roughly beyond 8.5 μm). They placed the CF wavelengths of different types of carbonaceous chondrites within the region between about 8.7 and 9.4 μm. The CO and CO3 types of the carbonaceous (Fig. 6) come closest in CF similarity with the 65 Cybele emittance peak between 9.0 and 9.4 μm, but the data quality is not sufficient for a conclusive identification. The two CO3 stony meteorites in Fig. 6 are Isna (upper curve) and ALHA 77003 (lower curve), the CO meteorites are Lance (2×), ALH 83108, Ornans and Warrenton (Salibury et al. 1991a). The CI and CM subclasses show the CF at slightly shorter wavelengths.

Our results from the emissivity analysis (Sect. 4.2) pointed at predominantly larger particles as cause for the far-IR emissivity drop. But the Salibury et al. (1991a) library provides only spectra of small grain sizes. Le Bras & Erard 2003 found that the grain size effect can shift the CF in wavelengths and change also the contrast. Meteoritic samples with larger grain sizes are therefore needed to proove direct connections between the measured spectroscopic features on asteroids and meteoritic samples.

For the feature between 12.5 and 14 μm we found no counterpart yet, but phyllosilicates, like Kaolinite, Lepidolite or Serpentine, show emissivity increases at around 12.5 μm, similar to what we see here. The fine-grained phyllosilicates are one main component of CI/CM carbonaceous chondrites, while the CO types are anhydrous materials. This would be an argument in favour of similarities with CI or CM types, but again, laboratory studies at larger grain sizes are needed to clarify the situation.

Figure 6 clearly reveals the difficulties of identifying mineralogic features based on mid-IR spectroscopy. Laboratory spectra of different meteorites at various grain sizes would be necessary. Concerning the observations of asteroids, a high S/N ratio over a large wavelengths range is necessary to detect the low level emissivity changes. These features would be very difficult to detect from ground-based N-band spectroscopy (8 to 13 μm) where atmospheric effects limit the wavelength range and degrade the data quality. Additional complications arise from the strong slope changes around the thermal continuum energy peak at around 14 μm. Poor spectral information together with wrongly modelled continuum slopes can then easily lead to misinterpretation at the band borders. The modelling of the surface temperature distribution, the thermal inertia as well as the beaming parameters ρ and f influence the slope of the thermal emission. Our thermal values (Sect. 3.1) worked perfectly for the PHT-S and the CAM-CVF data sets, but the spectroscopic interpretation still remains difficult.

4.4. Comparison with the STM

The shape and spin vector information is very important for a consistent analysis of the combined observations. Although we only used a simple ellipsoidal shape model, one can see the shape influence by comparing Fig. 7 with Fig. 4 in Sect. 4.1. For Fig. 7 we calculated the model values via the STM (Lebofsky et al. 1986), using a spherical shape model. The scatter between data sets taken under different aspect angles is much larger. Some measurements which agree in Fig. 4 are now offset by large amounts (e.g. the IRAS 12 and 25 μm observations and the CAM filter measurements). Assuming a spherical shape (with the given spin vector and thermal behaviour) leads to a weighted mean diameter of 280.0 km and an albedo of 0.047. But now the standard deviations would increase by about 60% for the diameter and about 50% for the albedo! This result clearly demonstrates the importance of using spin vector and shape information for combining observations from different epochs. Modifying the STM beaming value might improve the "Observation/STM" ratios for some observations, but different observations would require then different STM beaming values. And, for some data sets the STM would require a wavelength dependent η to account for the trends in Fig. 7.

We used the most reliable data set – the CAM filter measurements – for a comparison between TPM and STM radiometric results. The TPM analysis leads to a constant diameter and albedo value for all CAM filter measurements, while the STM produces wavelength dependent values (Fig. 8). The albedo values show the opposite behaviour. The derived diameters show no trend with wavelengths (see also Fig. 2, lower part for a comparison of the observation to TPM ratios over wavelengths) and agree within 2−3% (about 6% for the albedo). This also confirms our simplified constant emissivity values in this wavelength range close to the thermal emission peak. Simulations of the 65 Cybele constellation during the CAM filter epoch show that this wavelength dependent trend continues out to about 30 μm. At longer wavelengths also the STM would produce an almost constant diameter. At 30 μm the STM diameter would be about 10% larger. This wavelength dependent

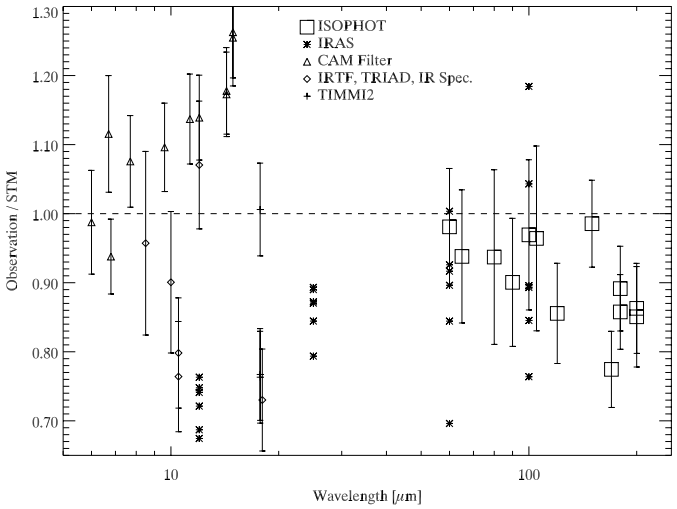

Fig. 7. The observation over STM ratios for the photometric measurements plotted against the corresponding wavelengths (see Fig. 4 for TPM ratios). All STM calculations were done with the resulting weighted mean values from Table 6.

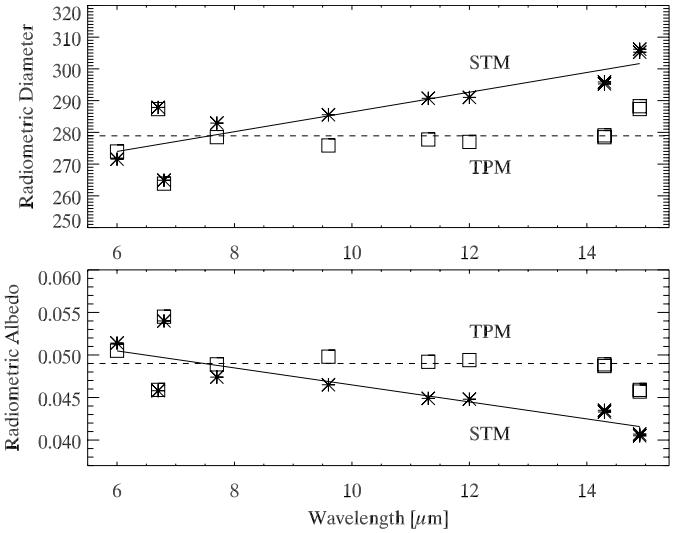

Fig. 8. The derived diameters and albedos for the CAM filter measurements as a function of wavelength, for the TPM and also the STM.

effect of the STM is mainly produced by the STM correction factor for infrared beaming. Detailed studies of the beaming influence with wavelengths and phase angles can be found in Müller (2002).

Figures 4, 5 and 7 reveal additional problems of the STM. The scatter in the observed fluxes divided by model calculations is much larger for the STM (Fig. 7). The main reason for the larger scatter is the assumption of a spherical shape. But also the simplified beaming, emissivity and phase angle corrections can be recognized in Figs. 4 and 7. The residual beaming effects cause wavelengths dependent ratios in Fig. 7, easily visible for the IRAS data (⋆-symbol) or the CAM filter data (△-symbol). The offset between these 2 sets is caused by the wrong cross section due to the spherical shape model of STM. The STM calculation of the ratios of Fig. 5 shows a strong asymmetry between the ratios before and after opposition. Additionally, the scatter between the different data sets would be much larger. Unfortunately, the overlaying shape effects of the inhomogeneous data did not allow to compare the 0.01 mag/° phase angle correction factor of the STM with the more sophisticated calculations of the true illumination and observing geometry by the TPM.

5. Conclusions

The recently developed TPM allows to combine thermal infrared observations with information from visual photometry, lightcurves, close-up observations or direct measurements. Using 65 Cybele as a "text book example", we applied this powerful TPM in several different ways. First, we used recalibrated observations from literature and recently obtained thermal infrared measurements to derive the size and albedo of 65 Cybele, taking also shape and spin vector information into account. Our derived effective diameter (273.0 ± 11.9 km) and albedo values (0.050 ± 0.005) deviate significantly from the IRAS based results of 237.3 ± 4.2 km and 0.071 ± 0.003 (Tedesco et al. 2002). We attribute these differences to the limitations of the STM (Sects. 4.1, 4.2 and 4.4).

The spectroscopic analysis confirmed the proposed "default thermal behaviour" (Müller et al. 1999) for large main-belt asteroids which is dominated by a surface regolith with very low thermal inertia. The related beaming model and thermal inertia values are the key elements to match even the high accuracy ISO measurements at the critical mid-IR range. In return, reliable diameter and albedo values can be determined from individual filter measurements at any thermal infrared wavelength. No band-to-band or wavelength dependent correction factors are necessary anymore. Additionally, the thermal emission modelling provides the basis for the analysis of mineralogic features and allows to investigate relations to meteoritic samples.

Acknowledgements. We would like to thank U. Klaas and P. Abraham for their support in the PHT-S data analysis and D. Osip for the provision of the IRTF observations. R. Siebenmorgen and M. Sterzik supported the ESO observing run and the data analysis of the TIMMI2 measurements. The ISOPHOT data presented in this paper were reduced using PIA, which is a joint development by the ESA Astrophysics Division and the ISOPHOT Consortium with the collaboration of the Infrared Processing and Analysis Center (IPAC). Contributing ISOPHOT Consortium institutes are DIAS, RAL, AIP, MPIK, and MPIA. The ISOCAM data presented in this paper were analysed using "CIA", a joint development by the ESA Astrophysics Division and the ISOCAM Consortium. The ISOCAM Consortium is led by the ISOCAM PI, C. Cesarsky. We also thank the referee Dr. Delbo for his careful review.

References

Ábrahám, P., Leinert, C., Acosta-Pulido, J. A., et al. 1999, in The Universe as seen by ISO, ed. M. F. Kessler, & P. Cox, ESA SP-427, 145

Barucci, M. A., Capria, M. T., Coradini, A., & Fulchignoni, M. 1987, Icarus, 72, 304

Barucci, M. A., Dotto, E., Brucato, J. R., et al. 2002, Icarus, 156, 202

Beichman, C. A., Neugebauer, G., Habing, H. J., Clegg, P. E., & Chester, T. J. 1988, Infrared Astronomical Satellite (IRAS), Catalogs and Atlases, Explanatory Supplement, NASA RP-1190, 1

Blommaert, J. A. D. L., Metcalfe, L., Altieri, B., et al. 2000, Experimental Astronomy, 10, 241

Blommaert, J. A. D. L., Okumura, K., & Boulanger, F. 2001, ISO Internal Rep., http://www.iso.vilspa.esa.es/

Bowell, E., Gehrels, T., & Zellner, B. 1979, in Asteroids, ed. T. Gehrels (University of Arizona Press), 1108

Bus, S. J. 1999, Ph.D. Thesis, Massachusetts Institute of Technology

Cesarsky, C. J., Abergel, A., Agnese, P., et al. 1996, A&A, 315, L32

Cohen, M., Witteborn, F. C., Walker, R. G., Bregman, J. D., & Wooden, D. H. 1995, AJ, 110, 275

Cohen, M., Walker, R. G., Carter, B., et al. 1999, AJ, 117, 1864

Coulais, A., & Abergel, A. 2000, A&ASS, 141, 533

Dobrovol'skij, O. V. 1980, IAU Circ., 3439

Dotto, E., Müller, T. G., Barucci, M. A., et al. 2000, A&A, 358, 1133

Dotto, E., Barucci, M. A., Müller, T. G., et al. 2002, A&A, 393, 1065

Erikson, A. 2000, Ph.D. Thesis Freie Universität Berlin, DLR-Forschungsbericht 2000-37, ISSN 1434-8454

Gaffey, M. J., Bell, J. F., & Cruikshank, D. P. 1989, in Asteroids II, ed. R. P. Binzel, T. Gehrels, & M. Shapley Matthews (University of Arizona Press), 98

Gradie, J. C., Chapman, C. R., & Tedesco, E. F. 1989, in Asteroids II, ed. R. P. Binzel, T. Gehrels, & M. Shapley Matthews (University of Arizona Press), 316

Green, S. F., Eaton, N., Aitken, D. K., et al. 1985, Icarus, 62, 282

Hauser, M. G., Kelsall, T., Leisawitz, D., et al. 1998, COBE Ref. Pub. 98-A (Greenbelt, MD: NASA/GSFC), available in electronic format from the NSSDC

Hiroi, T., Zolensky, C. M., Zolensky, M. E., & Lipschutz, M. E. 1996, Meteor. Planet. Sci., 31, 321

Lagerkvist, C.-I., & Magnusson, P. 1990, A&AS, 86, 119

Lagerros, J. S. V. 1996, A&A, 310, 1011

Lagerros, J. S. V. 1997, A&A, 325, 1226

Lagerros, J. S. V. 1998, A&A, 332, 1123

Laureijs, R. J., Klaas, U., Richards, P. J., et al. 2002, The ISO Handbook: PHT–The Imaging Photo-Polarimeter, SAI-99-069/Dc, Version 2.0, http://www.iso.vilspa.esa.es/

Lebofsky, L. A., Sykes, M. V., Tedesco, E. F., et al. 1986, Icarus, 68, 239

Lebofsky, L. A., & Spencer, J. R. 1989, 128, in Asteroids II, ed. Binzel, Gehrels, & Shapley Matthews (Arizona University Press)

Le Bras, A., & Erard, S. 2003, Planetary and Space Science, 51, 281

Lemke, D., Klaas, U., Abolins, J., et al. 1996, A&A, 315, L64

Morrison, D., & Chapman, C. R. 1976, ApJ, 204, 934

Morrison, D. 1977, ApJ, 214, 667

Müller, T. G., & Lagerros, J. S. V. 1998, A&A, 338, 340

Müller, T. G., Lagerros, J. S. V., Burgdorf, M., et al. 1999, in The Universe as Seen by ISO, ed. Cox, & Kessler, ESA SP-427, 141

Müller, T. G., & Lagerros, J. S. V. 2002, A&A, 381, 324

Müller, T. G. 2002, M&PS, 37, 1919

Ott, S., Abergel, A., Altieri, B., et al. 1997, in Astronomical Data Analysis Software and Systems (ADASS) VI, ed. G. Hunt, & H. E. Payne, ASP Conf. Ser., 125, 34

Redman, R. O., Feldman, P. A., Matthews, H. E., Halliday, I., & Creutzberg, F. 1992, AJ, 104, 405

Redman, R. O., Feldman, P. A., & Matthews, H. E. 1998, AJ, 116, 1478

Reimann, H.-G., Linz, H., Wagner, R., et al. 2000, Proc. SPIE, 4009, 440

Rieke, G. H., Lebofsky, M. J., & Low, F. J. 1985, AJ, 90, 900

Robberto, M., & Herbst, T. M. 1998, Proc. SPIE, 3354, 711

Salibury, J. W., D'Aria, D. M., & Jarosewichi, E. 1991a, Icarus, 92, 280

Salisbury, J. W., Walter, L. S., Vergo, N., et al. 1991b, Infrared spectra of minerals (Baltimore: Johns Hopkins Univ. Press)

Schober, H. J., Scaltriti, F., Zappala, V., & Harris, A. W. 1980, A&A, 91, 1

Simpson, J. P., Cuzzi, J. N., Erickson, E. F., et al. 1981, Icarus, 48, 230

Storrs, A., Weiss, B., Zellner, B., et al. 1999, Icarus, 137, 260

Taylor, G. E. 1981, J. British Astronomical Association, 92, 13

Tedesco, E. F., & Veeder, G. J. 1992, The IRAS Minor Planet Survey, Phillips Laboratory, 243

Tedesco, E. F., Noah, P. V., Noah, M., & Price, S. D. 2002, The Supplemental IRAS Minor Planet Survey, AJ, 123, 1056

Tholen, D. J. 1989, in Asteroids II, ed. R. P. Binzel, T. Gehrels, & M. Shapley Matthews (University of Arizona Press), 1139

Xiu-Yi, Y., et al. 1979, Astronomical Circular (China), No. 6